Applied Catalysis B: Environmental 142–143 (2013) 89–100

Contents lists available at SciVerse ScienceDirect

Applied Catalysis B: Environmental

journal homepage: www.elsevier.com/locate/apcatb

Influence of ceria on the NO_x reduction performance of NO_x storage reduction catalysts

Zafer Say[a], Evgeny I. Vovk[a,b], Valerii I. Bukhtiyarov[b], Emrah Ozensoy[a,*]

[a] Department of Chemistry, Bilkent University, 06800 Ankara, Turkey
[b] Boreskov Institute of Catalysis, 630090 Novosibirsk, Russian Federation

ARTICLE INFO

Article history:
Received 23 February 2013
Received in revised form 26 April 2013
Accepted 30 April 2013
Available online 8 May 2013

Keywords:
CeO_2
BaO
Pt, NO_x
NSR.

ABSTRACT

Influence of ceria on the NO_x storage and reduction behavior of NSR catalysts was investigated in a systematic manner over γ-Al_2O_3, Ba/Al, Ce/Al, Ba/Ce/Al, Pt/Al, Pt/Ce/Al and Ba/Pt/Ce/Al systems using BET, XRD, Raman spectroscopy and in situ FTIR. Although ceria promotion does not seem to have a substantial influence on the overall NO_x storage capacity, it does have a clearly positive effect on the NO_x reduction via H_2(g) during catalytic regeneration under rich conditions which is associated with the enhancement in the total amount of activated hydrogen on the catalyst surface and lowering of the thermal threshold for hydrogen activation. A strong metal support interaction (SMSI) between Pt sites and the BaO_x/CeO_x domains leads to a complex redox interplay including oxidation of the precious metal sites, reduction of ceria, formation of BaO_2 species as well as the formation of Pt–O–Ce interfacial sites on the Ba/Pt/Ce/Al surface. Ceria domains also act as anchoring sites for Pt species, limit their surface diffusion, enhance dispersion and hinder sintering at elevated temperatures. On the Ba/Pt/Ce/Al catalyst surface, reduction of the stored nitrates under relatively mild conditions via H_2(g) initially leads to the formation of surface –OH and –NH_x species and gas phase N_2O, as well as the destruction of surface nitrate species, leaving bulk nitrates mostly intact. Reduction proceeds with the conversion of N_2O(g) into N_2(g) along with the partial loss of surface –OH and –NH_x groups, dehydration and the loss of bulk nitrates.

1. Introduction

NO_x emissions from mobile sources have seriously destructive effects on the atmosphere, global ecosystem and especially on the human health. Due to the rigorous environmental regulations, automotive industry is compelled to search for new technologies to minimize the exhaust emissions. Three-way catalysts (TWC) are commonly used for the reduction of toxic gases in conventional gasoline engines which operate with an air to fuel ratios (A/F) close to 14.5. For a better fuel economy, diesel and lean burn gasoline engines have been considered as attractive alternatives that can operate at higher A/F. For lean burn engines, a promising after treatment method for the catalytic NO_x reduction is the NO_x storage/reduction (NSR) catalyst technology [1,2]. NSR catalysts consist of three main components. These are the NO_x storage component based on alkaline and alkaline earth oxides (e.g. K, Ba, Sr), precious metal sites (e.g. Pt, Pd, Rh) which are responsible for the oxidation and reduction, and the high surface area support material (e.g. γ-Al_2O_3) [3]. γ-Al_2O_3 is the most commonly used oxide support in NSR formulations due to its porous structure, high surface area as well as its distinct chemical, mechanical and thermal properties [4,5]. Former studies have shown that CeO_2 can be used either as a promoter [6] or as a support material [7] in TWC and NSR systems. The primary function of ceria stems from its favorable redox properties as well its high oxygen storage and transport capacity, which is associated with the facile transition between the two different Ce oxidation states (i.e. $Ce^{3+} \leftrightarrow Ce^{4+}$) and the presence of oxygen vacancies in its lattice structure. Ceria is also a very efficient promoter in the water-gas shift (WGS) and steam reforming reactions that are also relevant for exhaust emission control systems [8–11]. In addition, ceria has been reported to enhance the precious metal dispersion [12].

The primary aim of the current work is to study ceria-promoted NSR catalysts in order to elucidate the influence of ceria on the NO_x storage and reduction pathways at the molecular level. In order to achieve this goal, we focus our attention on the Ba/Pt/Ce/Al NSR catalysts and elucidate the structure and the catalytic behavior of this complex system by systematically analyzing its structural subcomponents, such as γ-Al_2O_3, Ba/Al, Ce/Al, Ba/Ce/Al, Pt/Al, Pt/Ce/Al.

2. Experimental

2.1. Catalyst synthesis

Binary CeO_2/Al_2O_3(Ce/Al) materials were synthesized by incipient wetness impregnation of γ-Al_2O_3 (PURALOX, 200 m^2/g, SASOL

* Corresponding author. Tel.: +90 3122902121.
E-mail address: ozensoy@fen.bilkent.edu.tr (E. Ozensoy).

0926-3373/$ – see front matter © 2013 Elsevier B.V. All rights reserved.
http://dx.doi.org/10.1016/j.apcatb.2013.04.075

GmbH, Germany) with $Ce(NO_3)_3{\cdot}6H_2O$ (>99.0%, Fluka, France) followed by calcination at 823 K for 2 h in air. Ce/Al material (denoted as 20Ce/Al) was prepared with a 20 wt% CeO_2 loading.

The $BaO/CeO_2/Al_2O_3$ (Ba/Ce/Al) ternary oxides with 8 and 20 wt% BaO loading were synthesized by the further impregnation of the 20Ce/Al samples (which were initially calcined at 823 K for 2 h in air) with aqueous solutions of barium nitrate ($Ba(NO_3)_2$, ACS Reagent, ≥99%, Riedel-de Häen, Germany). Next, resulting Ba/Ce/Al materials were annealed in Ar(g) flow at various temperatures within 323–1273 K as described in the text. For the synthesis of 1 wt% Pt-containing Pt/Al and Pt/20Ce/Al materials, γ-Al_2O_3 (as is) or 20Ce/Al (which was initially calcined at 823 K for 2 h in air) was impregnated with a solution of $Pt(NH_3)_2(NO_2)_2$ (Aldrich, diamminedinitritoplatinum(II), 3.4 wt.% solution in dilute NH_3(aq)). After impregnation, Pt/Al and Pt/20Ce/Al samples were annealed in Ar(g) flow at various temperatures within 323–1273 K.

$BaO/Pt/Al_2O_3$ (20Ba/Pt/Al) samples with 20 wt% BaO loading was synthesized by the impregnation of the Pt/Al samples (which were initially calcined at 823 K for 2 hr in air) with a $Ba(NO_3)_2$ solution followed by annealing in Ar(g) flow at various temperatures within 323–1273 K.

Similarly, $BaO/Pt/CeO_2/Al_2O_3$ (Ba/Pt/20Ce/Al) samples with 8 or 20 wt% BaO loading were synthesized by the impregnation of the Pt/20Ce/Al samples (which were initially calcined at 823 K for 2 h in air) with a $Ba(NO_3)_2$ solution followed by annealing in Ar(g) flow at various temperatures within 323–1273 K.

2.2. Instrumentation

The XRD patterns were recorded using a Rigaku Miniflex diffractometer, equipped with a Miniflex goniometer and an X-ray source with Cu Kα radiation (λ = 1.54 Å, 30 kV, 15 mA). The powder samples were pressed and affixed onto standard-sized glass slides and scanned within the 10–80°, 2θ range with a scan rate of $0.01^\circ\,s^{-1}$. Diffraction patterns were assigned using Joint Committee on Powder Diffraction Standards (JCPDS) cards supplied by the International Centre for Diffraction Database (ICDD).

The Raman spectra were recorded under ambient conditions using a HORIBA Jobin Yvon LabRam HR 800 instrument, equipped with a confocal Raman BX41 microscope, spectrograph with an 800 mm focal length and a CCD detector. The Raman spectrometer was equipped with a Nd: YAG laser (λ = 532.1 nm). While the Raman experiments were conducted, the laser power was tuned to 20 mW. All of the powder samples were mechanically dispersed onto a single-crystal Si holder. The incident light source was dispersed by a holographic grating with 600 grooves/mm and focused onto the sample using a ×50 objective. The confocal hole and slit entrance were set at 1100 and 200 μm, respectively. The spectrometer was regularly calibrated by adjusting the zero-order position of the grating and comparing the measured Si Raman band frequency with the typical reference value of 520.7 cm^{-1}. All Raman spectra were acquired within 100–4000 cm^{-1} with an acquisition time of 213 s and a spectral resolution of 4 cm^{-1}.

BET specific surface area (SSA) data were recorded usinga Micromeritics Tristar 3000 surface area and pore size analyzer via N_2(g) adsorption at 77 K. Prior to the BET measurements, materials were outgassed in vacuum at 623 K for 2 h.

FTIR spectroscopic measurements were carried out in transmission mode, in a batch-type catalytic reactor coupled to a FTIR spectrometer (Bruker Tensor 27). All of the FTIR spectra were collected at 323 K. Before the FTIR experiments, all of the samples were activated in the IR cell by exposing the sample surfaces to 2 Torr NO_2(g) for 5 min at 323 K followed by annealing in vacuum (<10^{-3} Torr) at 973 K. NO_2 adsorption on the synthesized materials was carried out typically by dosing 5.0 Torr NO_2(g) over the sample surface for 10 min at relevant temperatures (i.e. 323, 473, 523, 573 or 623 K). After the NO_2 exposure, the reactor was evacuated and the sample was cooled to 323 K. For the NO_x reduction experiments via H_2(g) (Linde GmbH, Germany,>99.9%), 15.0 Torr of H_2(g) was introduced into the reactor at 323 K and the sample was heated using a constant heating rate of 12 K/min until the desired temperature was reached. Next, samples were kept in H_2(g) at this temperature for 30 min in order to let the reduction proceed.

NO_2(g) used in the experiments were prepared by mixing NO(g) (Air Products, 99.9%) and O_2(g) (Linde GmbH, Germany, 99.999%) followed by multiple freeze-pump-thaw cycles for further purification.

Temperature programmed reduction (TPR) experiments were performed at General Motors Technical Center (Warren, MI) using a Micromeritics Autochem II 2920 analyzer equipped with a thermal conductivity detector (TCD). Prior to the TPR measurements, each catalyst sample (c.a. 100 mg) was pretreated in 10% O_2 in He for 1 h at 400 °C. The gas mixture for TPR was comprised of 10% of H_2 balanced with Ar, and the gas flow rate was fixed at 50 ml/min. The temperature was increased from room temperature to 600 °C with a heating rate of 10 °C/min and the effluent stream was monitored using a TCD.

3. Results and discussion

3.1. Structural characterization of the synthesized samples via BET, Raman spectroscopy and XRD

Fig. 1 shows BET specific surface area (SSA) values of the samples after calcination at various temperatures. It is visible in Fig. 1a that incorporation of γ-Al_2O_3 (having a typical SSA of 210 m^2/g) with CeO_2 and/or BaO decreases the SSA. Calcination of the synthesized samples at higher temperatures monotonically decreases the SSA which can be associated with ordering of the surface domains and sintering. It is apparent in Fig. 1b that SSA of Pt/Al sample reveals a relatively higher thermal stability with respect to all other samples that contain BaO and/or CeO_2. Comparison of the SSA values of the 20Ba/Pt/Al sample with that of the 20Ba/Pt/20Ce/Al samples suggests that ceria promotion leads to a noticeable decrease in the SSAs of the NSR catalysts after calcination at elevated temperatures.

Fig. 2 illustrates the ex situ Raman spectra acquired after the calcination of the synthesized 20Ce/Al, Pt/20Ce/Al and 20Ba/Pt/20Ce/Al samples at various temperatures in order to follow the structural evolution of these materials as a result of compositional variations and thermal effects. The most dominant Raman band observed in Fig. 2 appears at 460–465 cm^{-1}. This characteristic band has also been previously observed for pure CeO_2 and assigned to the Raman active *F2g* mode of the CeO_2 fluorite structure [13]. It is also worth mentioning that the main CeO_2 Raman signal also displays an asymmetry toward low frequencies revealing a shoulder at c.a. 400 cm^{-1} which can be attributed to defects [14]. On the other hand, very weak second order ($A_{1g} + E_g + F_{2g}$) Raman scattering features of CeO_2 are barely visible at 594 and 1170 cm^{-1} for the 20Ce/Al sample (Fig. 2a). Raman signals located at 740 and ~1050 cm^{-1} in Fig. 2a and c correspond to the bending and the symmetric stretching modes of NO_3^- species originating from the metal nitrate precursors ($Ce(NO_3)_3{\cdot}6H_2O$ and $Ba(NO_3)_2$ used in the synthesis, respectively [15]. These nitrate bands gradually disappear after elevated temperature treatments as a result of the decomposition of metal nitrates yielding peroxide (O_2^{2-}) species with a characteristic Raman signal at c.a. 830 cm^{-1} [16]. Comparison of the 623 K spectra in Fig. 2a–c reveals that in the absence of Pt and Ba, nitrates on the Ce/Al sample have moderate stability and only partially decompose at 623 K. On the other hand, on the Pt/20Ce/Al sample (Fig. 2b), presence of Pt sites facilitate the nitrate decomposition where all of the nitrate species on the

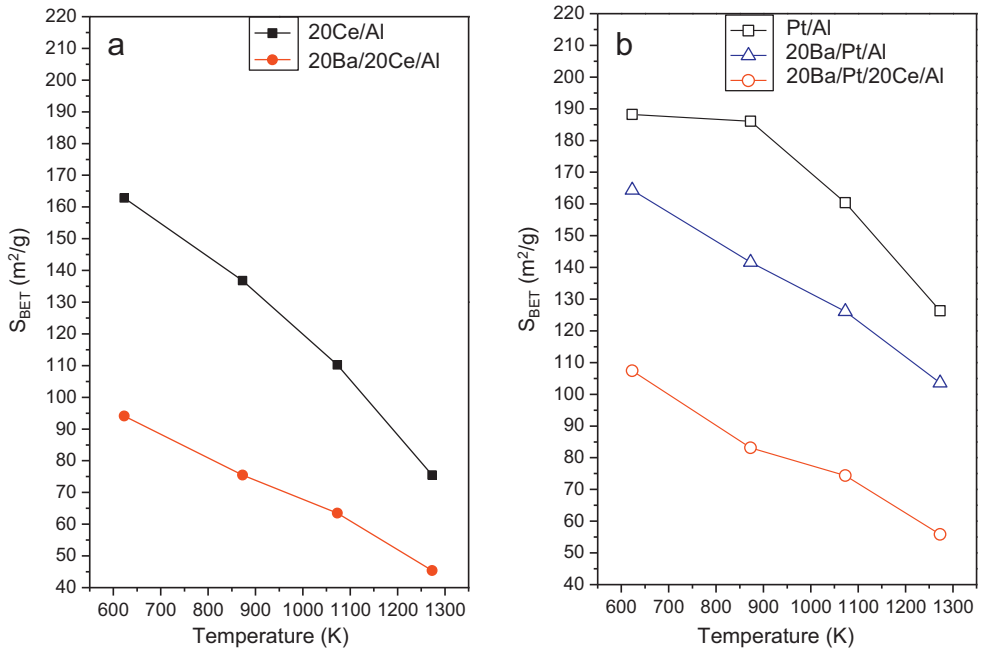

Fig. 1. BET specific surface area values for the analyzed samples upon annealing in Ar(g) flow within 623-1273 K. (a) 20Ce/Al(black) and 20Ba/20Ce/Al(red), (b) Pt/Al (black), 20Ba/Pt/Al (blue) and 20Ba/Pt/20Ce/Al (red). (For interpretation of the references to color in this figure legend, the reader is referred to the web version of this article.)

Pt/20Ce/Al surface can be completely destroyed at 623 K. Meanwhile, upon $Ba(NO_3)_2$ incorporation to the system (Fig. 2c), due to the higher thermal stability of barium nitrates, even in the presence of Pt, completion of the nitrate decomposition process requires temperatures greater than 1073 K. Decomposition behavior of the metal nitrate precursors observed via current Raman experiments is in excellent agreement with the XRD data given in Fig. 3, where the decomposition of the ordered $Ba(NO_3)_2$ phase and the formation of an amorphous BaO/BaO_2 phase on the 20Ba/Pt/20Ce/Al surface (Fig. 3d) is clearly visible [17–19]. It is worth mentioning that although XRD data suggest that all of the nitrate species on the 20Ba/Pt/20Ce/Al surface seem to be decomposed at 873 K (Fig. 3d), owing to the higher sensitivity of the Raman spectroscopy, corresponding Raman data (Fig. 2c) reveals the existence of nitrates at $T \leq 1073$ K.

Probably, the most important set of Raman features observed in Fig. 2 are the bands that arise after the addition of Pt to the synthesized materials. It is seen in Fig. 2b and c that the addition of Pt followed by annealing in Ar(g) flow at moderate temperatures ($T \leq 873$ K) leads to the appearance of a broad and a convoluted set of bands located within 500–700 cm^{-1}. These features become relatively sharper after elevated temperature treatments yielding signals at 205, 544, 582, and 689 cm^{-1}. Based on the former Raman spectroscopic studies on β-PtO_2 [20], 205 cm^{-1} feature can be assigned to the Raman active $A_g(\omega_1)$ mode of PtO_x and/or PtO_2. Similarly, in the light of the previous studies on Pt/CeO_2 [21], 544 and 689 cm^{-1} features can be attributed to the Pt–O–Ce species (located at the Pt/CeO_x interface) and a Pt–O signal associated with surface PtO_x/PtO_2 species, respectively. The remaining 582 cm^{-1} feature can be tentatively assigned to Pt–O–Ce species and/or the

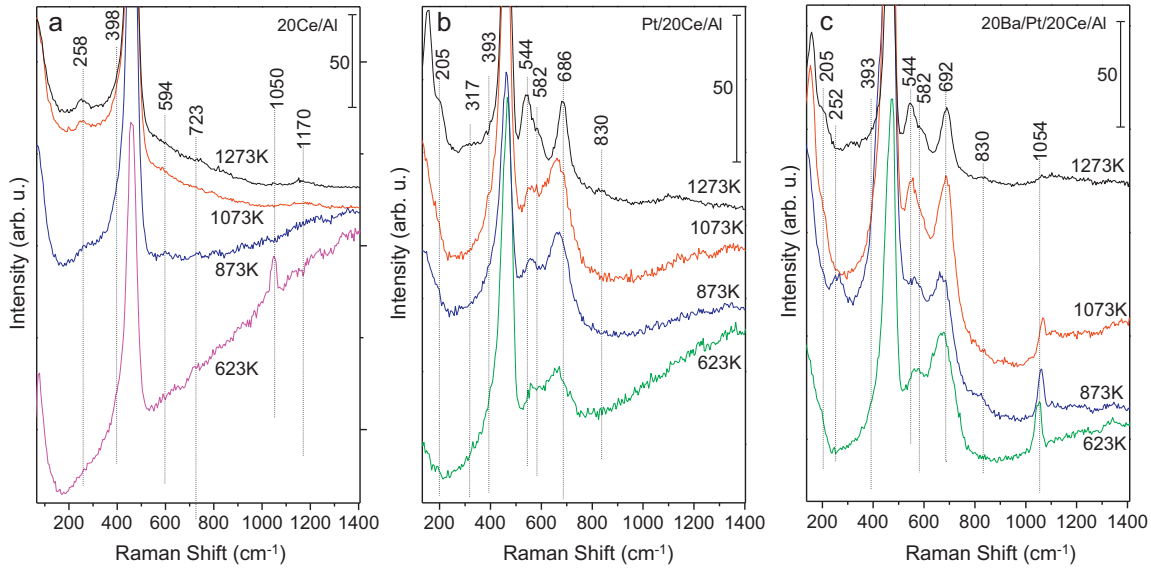

Fig. 2. Ex situ Raman spectra corresponding to (a) 20Ce/Al, (b) Pt/20Ce/Al and (c) 20Ba/Pt/20Ce/Al samples upon annealing in Ar(g) flow within 623–1273 K.

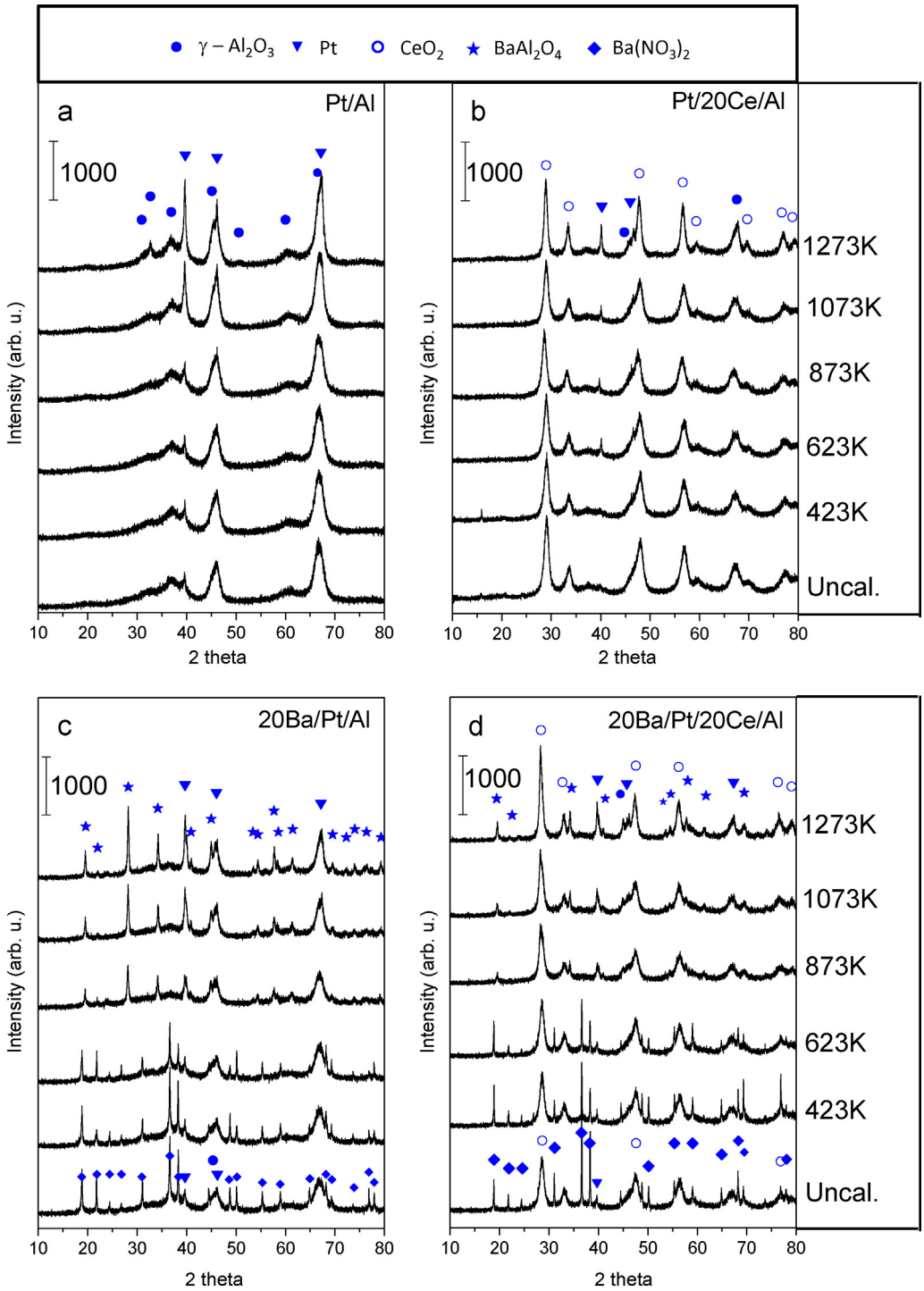

Fig. 3. Ex situ XRD patterns corresponding to (a) Pt/Al, (b) Pt/20Ce/Al, (c) 20Ba/Pt/Al and (d) 20Ba/Pt/20Ce/Al samples upon annealing in Ar(g) flow within 623–1273 K.

second order ($A_{1g} + E_g + F_{2g}$) Raman scattering features of CeO_2. It is worth mentioning that metallic Pt is not Raman active [21]. Thus, metallic Pt species were not detected in the current Raman spectroscopic measurements; although presence of such species are shown in complimentary XRD measurements given in Fig. 3.

Current Raman spectroscopic results clearly point out a strong interaction between the precious metal (Pt) sites and the underlying reducible metal oxide support (CeO_2), evident by the existence of Pt–O–Ce species which are formed due to the strong metal support interaction (SMSI) [22–28]. SMSI is known to be triggered by the partial reduction of the reducible oxide support (i.e. CeO_2) which is initiated by the action of a precious metal (i.e. Pt) [29]. This leads to the formation of a partially reduced overlayer of the support material, demonstrating an unusually high affinity toward the precious metal. As a result, partially reduced metal oxide layer binds strongly to the precious metal sites and can even migrate over these sites to cover them [8–10,30]. SMSI can have contrasting implications on the catalytic performance [29]. In the case where the precious metal sites are completely covered and buried by the metal oxide overlayer, catalytic activity of the overall system can be lost in a significant manner [8]. Such a loss in the catalytic activity also renders itself as a drastic decrease in the typical CO(g) and

H_2(g) adsorption capacities of the corresponding catalyst surfaces. Alternatively, if the reduced metal oxide overlayer only partially covers the precious metal sites, new active sites can be generated at the metal/metal oxide boundary. These newly formed interfacial sites can radically boost the catalytic activity of the system [8], as in the case of the water-gas shift (WGS) reaction where the formation of such sites has been recently reported to increase the WGS performance by up to 20 folds [9] as a result of the unusual activity of the Pt/CeO_x interfacial system toward H_2O dissociation accompanied by the stabilization of the dissociation products. Clearly, currently investigated Pt/20Ce/Al and 20BaPt/Ce/Al systems do also reveal potent Pt–O–Ce sites that may present important catalytic implications on the NO_x storage and NO_x reduction via H_2(g).

In a recent Raman and Infrared spectroscopic study on the Pt/CeO_2 system [21], it has been shown that in the presence of H_2(g), PtO_x/PtO_2 sites are reduced faster than CeO_2 (where CeO_2 reduction has been indirectly followed by monitoring the loss of the –OH (Type-I) vibrations at 3695 cm^{-1} in FTIR), leading to the formation of reduced Pt sites which can further trigger CeO_2 reduction by activation of hydrogen and hydrogen spill-over. The same study has also elegantly demonstrated that during the reoxidation of the initially reduced Pt/CeO_2 system with $^{18}O_2$(g), oxidation of the ceria support precedes the oxidation of the supported Pt phase. Thus, subsequent oxidation of the supported Pt phase is achieved by the ^{16}O species of the ceria lattice and not directly by $^{18}O_2$(g). In other words, the primary function of the O_2(g) during the oxidation process was suggested to be healing of the oxygen vacancies in the CeO_x/CeO_2 lattice.

In the light of these findings, ex situ Raman spectroscopic data corresponding to Pt/20Ce/Al (Fig. 2b) and 20Ba/Pt/20Ce/Al (Fig. 2c) samples can be analyzed in a comparative manner in order to gain further insight regarding the interaction between different metal oxide domains on the surface. It is apparent that the incorporation of BaO_x domains into the Pt/20Ce/Al system (for instance, compare 623 K spectra in Fig. 2b and 2c) results in the strengthening of the Pt–O–Ce (544 cm^{-1}) and Pt–O (692 cm^{-1}) signals. It is likely that the peroxide species that are formed during the decomposition of the metal nitrate precursors [16,31] can assist the oxidation of the Pt sites. This can also be accompanied by other additional oxidation routes, in which ceria can act as an oxygen reservoir and oxidize Pt sites. Alternatively, nitrates can also directly take part in the Pt oxidation during the thermal nitrate decomposition. In overall, current Raman data indicate the presence of various surface species such as PtO_x, Pt–O–Ce, CeO_x and O_2^{2-} which can directly take part in NO_x surface chemistry and are rather elusive to detect by other experimental techniques.

Fig. 3 shows ex situ XRD data for the Pt/Al (a), Pt/20Ce/Al (b), 20Ba/Pt/Al (c) and 20Ba/Pt/20Ce/Al (d) samples obtained after thermal treatment steps at different temperatures. XRD patterns in Fig. 3 show diffraction signals corresponding to the γ-Al_2O_3 (JCPDS 001-1303), CeO_2 (JCPDS 001-0800), $Ba(NO_3)_2$ (JCPDS 24-0053), $BaAl_2O_4$ (JCPDS 017-0306) and metallic Pt (JCPDS 001-1190) phases. It is important to note that although γ-Al_2O_3 → α-Al_2O_3 (corundum JCPDS 001-1296) phase transition can be observed at 1273 K for other binary mixed oxides of alumina such as TiO_2–Al_2O_3 [17,18] or Fe_2O_3–Al_2O_3 [19], corundum phase was not observed in the presence of ceria (Fig. 3). In a similar fashion, XRD signals corresponding to the oxidic phases of Pt such as PtO_2 (e.g. JCPDS 021-0613) was not visible in the current measurements.

Comparison of Fig. 3a and b indicates that the presence of ceria hinders the precious metal sintering and facilitates the dispersion of the Pt sites, as the major XRD signal of metallic Pt ($2\theta = 39.65^\circ$) species is broader and weaker on Pt/20Ce/Al with respect to that of Pt/Al. The same observation is also valid for the Ba-containing samples (Fig. 3c and 3d). For Ba-containing samples, a crystalline $Ba(NO_3)_2$ phase was detected at lower temperatures which decomposes into amorphous BaO/BaO_2 at $T \geq 873$ K [16]. Stabilization or immobilization of the Pt particles by a ceria substrate has been reported in former studies in the literature [23], where such an observation has been attributed to a strong Pt–CeO_2 interaction, anchoring the Pt sites on the ceria surface and preventing their sintering. For the Ba-containing samples in Fig. 3c and d, formation of a $BaAl_2O_4$ is also observed at elevated temperatures, which is one of the characteristic indicators associated with the thermal aging of conventional NSR catalysts at elevated temperatures [17–19].

3.2. Reduction of adsorbed NO_x species on Pt-free ceria promoted NSR materials via H_2(g)

The low-temperature NO_x uptake (via NO_2(g) adsorption) and the subsequent NO_x reduction behavior (via H_2(g)) of the prepared Pt-free NSR materials were investigated by in situ FTIR. In order to demonstrate the direct effect of the ceria domains on the NO_x reduction, in the absence of Pt and BaO sites, γ-Al_2O_3 and 20Ce/Al surfaces were investigated. Fig. 4 shows the FTIR spectra after the saturation of the γ-Al_2O_3 and 20Ce/Al surfaces with 5 Torr NO_2(g) for 10 min (black spectra) at 473 K, 523 K and 573 K as well as their subsequent reduction with H_2(g) at 473 K, 523 K and 573 K (red spectra). NO_x adsorption (black) spectra were acquired in vacuum while H_2 reduction (red) spectra were acquired in the presence of 15.0 Torr H_2(g). IR bands observed after saturation of the γ-Al_2O_3 with NO_2(g) have been discussed in previous reports [17,32–34] and can be assigned to various types of nitrates such as bridging (1650, 1620 and 1257 cm^{-1}), bidentate (1595 and 1290 cm^{-1}) and monodentate (1565 and 1298 cm^{-1}) nitrates. Line shapes of the FTIR spectra corresponding to NO_2-saturated 20Ce/Al surface (Fig. 4b) demonstrate a significant resemblance to that of the γ-Al_2O_3 surface (Fig. 4a). Reduction of the stored nitrates on γ-Al_2O_3 by H_2(g) at 473 K results in a minor decrease in the nitrate signals, while a more noticeable decrease was observed for 20Ce/Al under identical conditions. After reduction at 523 K, loss in the nitrate signals become pronounced for the γ-Al_2O_3 surface, while reduction still seems to occur at a much larger extent on 20Ce/Al. Reduction at 573 K leads to the complete loss of the nitrate species on the 20Ce/Al surface whereas nitrate bands are not completely eliminated for γ-Al_2O_3. Thus, Fig. 4 demonstrates that CeO_2 domains can directly facilitate NO_x reduction via H_2(g) on the 20Ce/Al system through the formation of oxygen vacancies [35]. Further insight regarding this point can be obtained by investigating the–OH/–NH stretching region of the corresponding FTIR spectra (Fig. 5).

–OH/–NH stretching region of the FTIR spectra corresponding to the γ-Al_2O_3 and 20Ce/Al samples upon NO_x saturation and subsequent reduction with H_2(g) is given in Fig. 5. These spectra present a complex set of convoluted IR features which are located at three different frequency windows namely, 3789–3695 cm^{-1}, 3695–3510 cm^{-1} and 3510–3000 cm^{-1}. Upon NO_2 adsorption on γ-Al_2O_3 and 20Ce/Al samples at 473–573 K, a group of characteristically sharp and negative IR signals were detected within the first frequency window at 3789, 3755, 3742, and 3695 cm^{-1}. These features reveal relatively invariant vibrational frequencies for both samples within 473–573 K and can be readily assigned to the so called Type I and Type II isolated hydroxyl groups [34,36]. In particular, 3695 cm^{-1} feature deserves special attention as the loss of this particular IR feature (i.e. observation of a negative peak at this frequency) was reported to be an indication of the reduction of the ceria domains [21]. However care should be taken regarding the analysis of this particular vibrational feature, since γ-Al_2O_3 surface also has isolated –OH species revealing an IR signature at this frequency. Thus, we analyzed γ-Al_2O_3 and 20Ce/Al samples in a comparative fashion in order to monitor the evolution of this particular band. Within the second frequency window in Fig. 5, very broad and convoluted IR features can be noticed (e.g. 3649 and

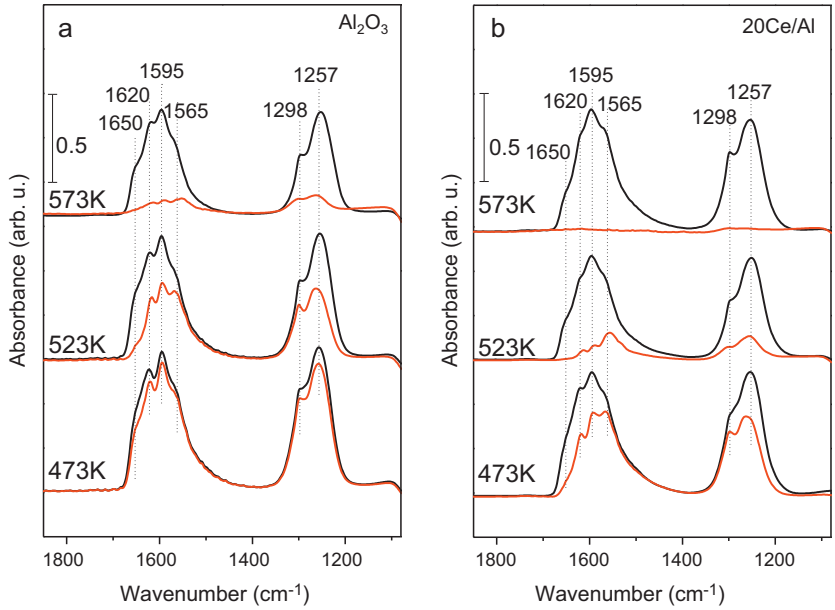

Fig. 4. In situ FTIR spectra corresponding to NO_2 adsorption and saturation (5.0 Torr NO_2(g), 10 min, black spectra) followed by subsequent reduction with H_2(g) (15.0 Torr H_2(g), 30 min, red spectra) at various temperatures on (a) γ-Al_2O_3 and (b) 20Ce/Al at 473, 523 and 573 K. All spectra were acquired at 373 K. Black spectra were acquired in vacuum while red spectra were obtained in H_2(g). (For interpretation of the references to color in this figure legend, the reader is referred to the web version of this article.)

3558 cm^{-1}). These poorly defined features can be attributed to H-bonded hydroxyl species [34,36]. Finally within the third frequency window, additional poorly resolved and broad features can also be discerned at 3384 and 3266 cm^{-1} which can be assigned to H-bonded hydroxyl species as well as –NH modes associated with –NH_2, –NH_3, –OH···NH_x or –OH···NO_x species [37,38].

It is visible in Fig. 5a that reduction of the γ-Al_2O_3 surface with H_2 at 473 K leads only to minor recovery of the isolated–OH species located at 3789, 3755 and 3742 cm^{-1}. On the other hand, in addition to the partial recovery of the isolated–OH species, onset of the–NH stretching signals (at 3384 and 3264 cm^{-1}) is also visible on the 20Ce/Al sample upon reduction at 473 K (Fig. 5d). This observation is in agreement with the FTIR data presented in Fig. 4, suggesting that ceria domains start to facilitate NO_x reduction even under mild reduction conditions. Reduction at higher temperatures results in a further increase in the –NH signals (at 3384 and 3264 cm^{-1}) for both samples. In addition, reduction of the 20Ce/Al sample (Fig. 5e and f) at higher temperatures also leads to the progressive growth of the negative bands at 3695–3711 and 3662 cm^{-1} which can be attributed to the reduction of the ceria lattice and the formation of oxygen vacancies. It can be argued that during the reduction of the NO_2-saturated γ-Al_2O_3 and 20Ce/Al surfaces, H_2 activation occurs more readily on the ceria promoted surface. During the initial stages of the reduction process, it is likely that basic surface sites (i.e. O^{2-}) are protonated forming isolated –OH species. This is accompanied by the interaction of surface –OH species with the adsorbed nitrates to yield surface species having –NH_x stretchings. Furthermore, hydrogen exposure at elevated temperatures also results in the partial reduction of the ceria lattice and the formation of oxygen vacancies on the 20Ce/Al sample.

As the next step, the structural complexity of the investigated systems is increased further by the incorporation of NO_x storage domains. Along these lines, NO_x adsorption and subsequent reduction via H_2(g) were investigated on Ba-containing samples (i.e. 20Ba/Al, 20Ba/20Ce/Al and 8Ba/20Ce/Al) in the absence of Pt (Fig. 6). These particular set of samples were analyzed in order to shed light on the influence of the ceria promotion on Pt-free NSR systems as a function of Ba-loading. FTIR spectra corresponding to the NO_2(g) adsorption on BaO/Al_2O_3 surface has been thoroughly analyzed in the literature [39–45]. In the light of these former studies, NO_2 adsorption signals (upon 5.0 Torr NO_2 exposure for 10 min at 473, 523, 573 or 623 K and subsequent evacuation at 323 K) in the FTIR experiments (Fig. 6a) corresponding to the 20Ba/Al sample can be assigned to bulk (ionic) Ba-nitrates (~1320, ~1440 and ~1480 cm^{-1}) and surface (bidentate) Ba-nitrate features (1585, 1565, 1300 cm^{-1}). Remaining nitrate bands at 1583 and ~1630 cm^{-1} are associated with bidentate and bridged nitrates, respectively.

Incorporation of ceria to the 20Ba/Al system (Fig. 6a and 6b) does not significantly alter the general line shapes of the FTIR spectra corresponding to the NO_2 adsorption at 473, 523 and 623 K. Upon reduction with H_2(g) (5.0 Torr, 30 min exposure for each reduction step) at 473 K and 523 K the most prominently observed change is the attenuation of the surface nitrate features. At $T \leq 523$ K (i.e. under mild reduction conditions), reduction occurs mostly on the surface of the NO_x storage domains, leaving bulk storage domains rather intact. These observations suggest that under these conditions, where the promotional effect of ceria is not operational in its full extent, relatively similar nitrate reduction pathways seem to be underway for the 20Ba/Al and 20Ba/20Ce/Al surfaces. On the other hand, reduction at 623 K reveals a different behavior (Fig. 6a and b). Although most of the adsorbed NO_x signals in the FTIR spectrum are lost for the 20Ba/20Ce/Al sample at 673 K, a noticeably larger NO_x signal is visible for the 20Ba/Al sample. Thus, upon activation of the ceria domains, NO_x reduction process is significantly facilitated. Activation of the ceria domains at elevated temperatures on the 20Ba/20Ce/Al surface is likely to be associated with the formation of oxygen vacancies in the ceria lattice as discussed earlier for the 20Ce/Al surface (Fig. 5f).

Influence of the Ba-loading on the NO_x storage and reduction on Pt-free Ba/Ce/Al ternary oxide systems can be discussed by comparing Fig. 6b and c. It is clear that a lower Ba loading results in weaker bulk-nitrate bands and stronger surface nitrate signals, consistent with the presumably smaller particle size of the Ba domains on the 8Ba/20Ce/Al surface. Surface Ba-nitrates are known to have lower stability with respect to that of the bulk Ba-nitrate species [18]. Along these lines, Fig. 6c clearly demonstrates that on the 8Ba/20Ce/Al surface, all of the nitrate species can be reduced almost

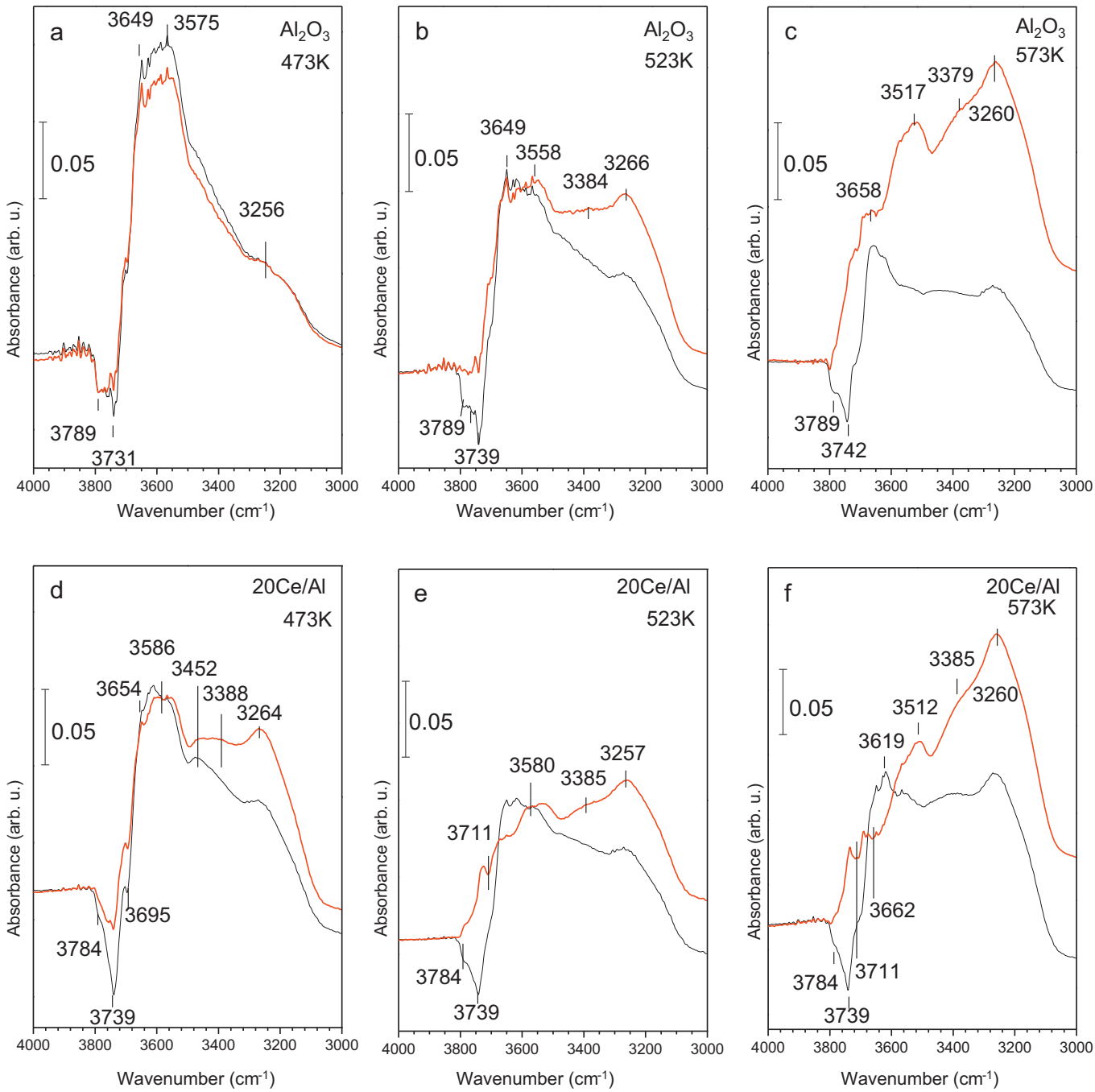

Fig. 5. –OH/–NH stretching region of the in situ FTIR spectra corresponding to NO_2 adsorption and saturation (5.0 Torr NO_2(g), 10 min, black spectra) followed by subsequent reduction with H_2(g) (15.0 Torr H_2(g), 30 min, red spectra) on γ-Al_2O_3 at (a) 473 K, (b) 523 K, (c) 573 K and on 20Ce/Al at (d) 473 K, (e) 523 K, (f) 573 K. Black spectra were acquired in vacuum while red spectra were obtained in H_2(g). (For interpretation of the references to color in this figure legend, the reader is referred to the web version of this article.)

fully with H_2 at 573 K, while on the 20Ba/20Ce/Al surface, some of the bulk nitrate species survive even at 623 K. This observation can be attributed to the larger NO_x storage capacity and the greater stability of nitrate species on the 20Ba/20Ce/Al surface, as well as the suppression of the promotional ceria sites due to high Ba surface concentration.

3.3. Reduction of adsorbed NO_x species on Pt-containing ceria promoted NSR materials via H_2(g)

Having investigated the influence of the ceria domains on the NO_x adsorption and subsequent reduction via H_2(g) over binary (Ce/Al and Ba/Al) and ternary (Ba/Ce/Al) oxide systems, we focused our attention on Pt-containing ceria promoted NSR systems. Rather than directly tackling with the complex 20Ba/Pt/20Ce/Al system, we performed initial benchmark studies on Pt/Al and Pt/20Ce/Al samples in order to gain systematic insight regarding the catalytic sub-components of the system of interest. Our preliminary NO_x saturation and reduction experiments on Pt/Al and Pt/20Ce/Al at $T \geq 473$ K (data not shown) revealed that nitrate reduction with 15 Torr H_2(g) is extremely fastover Pt/Al and Pt/20Ce/Al surfaces, readily removing nitrates from these surfaces and rendering their comparison rather difficult. Thus, in order to decelerate the reduction kinetics and demonstrate the

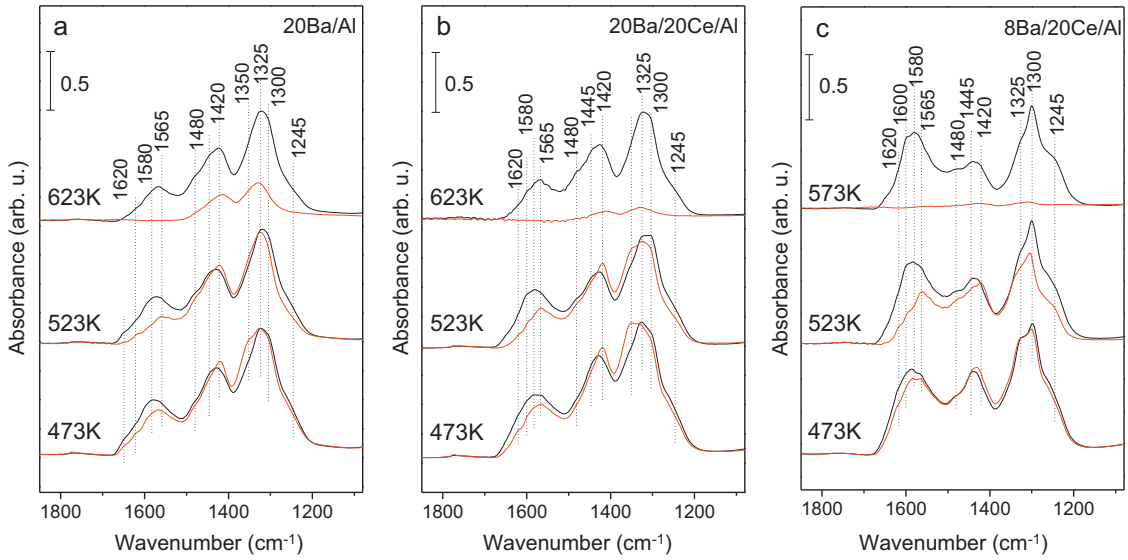

Fig. 6. In situ FTIR spectra corresponding to NO_2 saturation (5.0 Torr NO_2(g), 10 min, black spectra) followed by subsequent reduction with H_2(g) (15.0 Torr H_2(g), 30 min, red spectra) of (a) 20Ba/Al at 473 K, 523 K and 623 K, (b) 20Ba/20Ce/Al at 473 K, 523 K and 623 K, (c) 8Ba/20Ce/Al 473 K, 523 K and 573 K. All spectra were acquired at 373 K. Black spectra were acquired in vacuum while red spectra were acquired in H_2(g). (For interpretation of the references to color in this figure legend, the reader is referred to the web version of this article.)

differences between the relative reduction performances of Pt/Al and Pt/20Ce/Al surfaces, NO_2 adsorption and subsequent H_2 reduction experiments were performed at a lower temperature (i.e. at 323 K) and the reduction process was monitored as a function of time.

Fig. 7 illustrates the FTIR spectra obtained during these experiments. Black spectra in Fig. 7a and 7b were acquired immediately after the NO_2 adsorption on fresh Pt/Al and Pt/20Ce/Al surfaces at 323 K, respectively. After the saturation of the surfaces with NO_2(g), reduction process was initiated by the introduction of 15.0 Torr H_2(g) at 323 K and the time-dependent (red) FTIR spectra were acquired over the course of 4 hr. Blue spectra represent the final conditions at the end of the 4 hr period. Black spectrum for the Pt/Al sample in Fig. 7a is characterized by nitrate signals located at 1630 and 1255 cm^{-1} (bridging nitrates) and 1570 and 1300 cm^{-1} (monodentate nitrates). It is interesting that immediately after the introduction of H_2(g), a noticeable alteration in the adsorption geometry of the surface nitrate species is observed where bridging nitrates are partially converted into monodentate nitrates. Corresponding –OH/–NH stretching region (Fig. 7c) clearly shows that the transformation in the nitrate adsorption geometry is accompanied by the recovery of the isolated –OH species (3789, 3737 and 3696 cm^{-1}) and the growth of the H-bonded –OH (3531 cm^{-1}) and –NH (3450, 3384, 3282 cm^{-1}) species. This observation is consistent with the competition for the available surface adsorption sites between the adsorbed bridging nitrate species (requiring two vacant adsorption sites per adsorbate) and the reduction species that are produced after the introduction of H_2(g) enforcing adsorbed nitrates geometry change from bridging to monodentate configuration. It is also worth mentioning that the broad shoulder at 1500 cm^{-1} appearing in the presence of H_2 can be attributed to nitrite species which is formed as an intermediate during the nitrate reduction [46] while the feature at 1410 cm^{-1} can be assigned to bulk nitrates [32,46]. Increase in the bulk nitrate signal can be associated with the conversion of surface nitrates into bulk nitrates, induced by –OH/–NH species formed during the reduction process. Such a transformation has also been observed in former studies upon reduction or hydration of nitrated surfaces [42,46,47]. Fig. 7a and c shows that after 4 h reduction at 323 K, signals associated with H-bonded–OH species and the –NH signals continuously grow in intensity while nitrate signals attenuate. Clearly, these observations are consistent with the reduction of adsorbed NO_x species via H_2. It is apparent that under these mild reduction conditions, only a certain portion of the isolated hydroxyl species is recovered on the Pt/Al surface. Similarly, adsorbed nitrates are only partially reduced.

On the other hand, identical set of experiments performed on the Pt/20Ce/Al sample presents noteworthy differences (Fig. 7b and d). Although a similar set of vibrational features associated with NO_x species are observed on the Pt/20Ce/Al surface (Fig. 7b), time-dependent evolution of the intensities of these features are quite different. In overall, it is apparent that nitrate signals attenuate much faster on the Pt/20Ce/Al surface revealing the promotional effect of ceria in the NO_x reduction. Also Fig. 7c and d shows that the negative 3695 cm^{-1} feature which is associated with the reduced ceria domains, is more pronounced for the Pt/20Ce/Al surface than the Pt/Al sample. This suggests that the promotional effect of ceria can be associated with the oxygen vacancy formation in the partially reduced ceria domains.

As discussed above, our preliminary NO_x storage and reduction experiments on the γ-Al_2O_3, 20Ba/Al, 20Ba/20Ce/Al, 8Ba/20Ce/Al, Pt/Al, 20Ce/Al and Pt/20Ce/Al surfaces (Figs. 4-7) provide a valuable insight regarding the catalytic behavior of the key components constituting the complex 20Ba/Pt/Al and 20Ba/Pt/20Ce/Al systems. In the light of these preliminary experiments, NO_x storage and reduction phenomena on the 20Ba/Pt/20Ce/Al system can now be elucidated in detail.

Fig. 8 presents NO_2 adsorption (5.0 Torr NO_2(g) exposure for 10 min at 323 K, followed by evacuation) and reduction (15 Torr H_2(g) exposure for 4 hr at 323 K) experiments on the 20Ba/Pt/Al and 20Ba/Pt/20Ce/Al surfaces. Fig. 8a and 8b indicates that after NO_2 adsorption, nitrate features are detected at 1620 and 1260 cm^{-1} (bridging surface nitrates), 1560 and 1330 cm^{-1} (bidentate and/or monodentate surface nitrates) and 1420 cm^{-1} (bulk nitrates) [42,46,47]. Time-dependent FTIR spectra obtained after the introduction of H_2(g) on the 20Ba/Pt/Al and 20Ba/Pt/20Ce/Al surfaces at 323 K demonstrate an immediate change in the relative intensities of the surface and bulk nitrates, where surface nitrate signals decrease and the bulk nitrate signals increase. This observation is in agreement with the former experiments performed on ceria-free

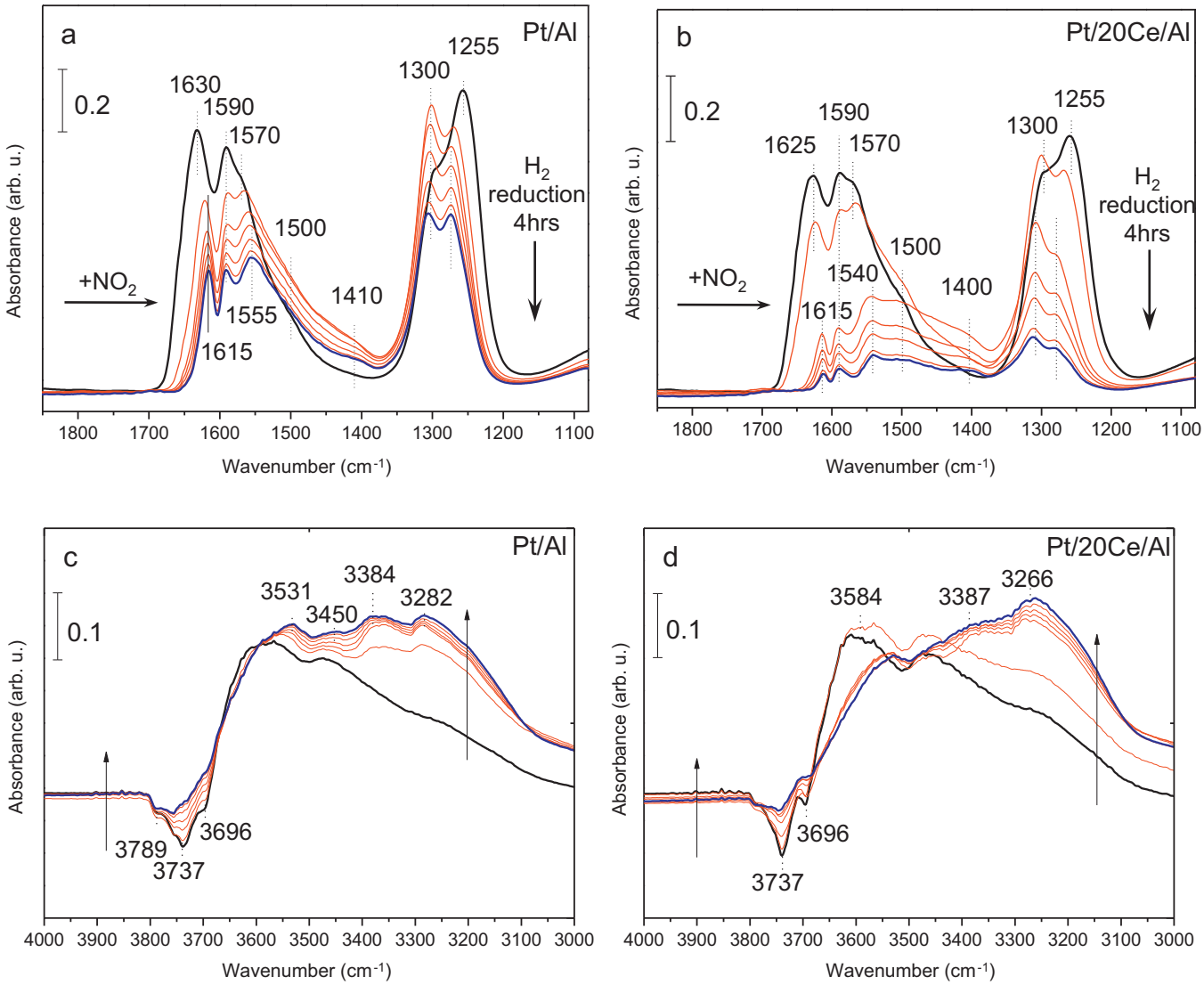

Fig. 7. Time-dependent in situ FTIR spectra corresponding to NO_2 saturation (5.0 Torr NO_2(g), 10 min, black spectra) followed by subsequent reduction with H_2(g) (15.0 Torr H_2(g), 3, 10, 30, 60, 120, 240 min, red spectra) on Pt/Al and Pt/20Ce/Al samples at 323 K. Blue spectra were obtained at the end of the 240 min reduction period. Panels (a) and (c) correspond to Pt/Al sample while panels (b) and (d) represent Pt/20Ce/Al sample. All spectra were acquired at 373 K. Black spectra were acquired in vacuum while red and blue spectra were acquired in H_2(g). (For interpretation of the references to color in this figure legend, the reader is referred to the web version of this article.)

NSR catalysts suggesting aggregation of the Ba domains [32,46]. After the initial minor spectral changes occurring in the first 60 min of reduction, the intensities of surface and bulk nitrate species on 20Ba/Pt/Al surface remain practically invariant until the end of 240 min reduction process. Meanwhile the intensity of surface and bulk nitrates on ceria-containing material monotonically decreases over the course of the 240 min reduction period at 323 K. Furthermore, the intensities of the nitrate related features substantially decrease after heating both materials at 473 K however the ceria promoted 20Ba/Pt/20Ce/Al material demonstrates a significantly stronger attenuation in nitrate features. After heating in hydrogen at 573 K the nitrates are almost completely eliminated from both materials. The presented data clearly point out that ceria promotion enhances the nitrate reduction performance of the conventional NSR catalyst.

–OH/–NH region of the corresponding FTIR spectra given in Fig. 8b and 8c also indicate that during the reduction, isolated –OH species are slightly recovered. Concomitant to this observation, intensities of the H-bonded –OH species as well as –NH species also increase during the reduction period. After these reduction experiments under mild conditions (i.e. at 323 K), surface temperature of the catalyst was increased to 473 K and subsequently to 573 K in the presence of H_2(g) in order to monitor the reduction phenomena under strongly reducing conditions (see blue spectra in Fig. 8). It is clearly visible in Fig. 8a that after reduction at 473 K, almost all of the surface nitrate signals disappear and the bulk nitrate signals attenuate significantly, indicating the facile elimination of the stored nitrates. –OH/–NH region of the corresponding FTIR spectra reveal a significant loss of –OH, –NH signals indicating the removal of the reduction intermediates/products and dehydroxylation. This is accompanied by the growth of a negative signal at 3695 cm^{-1} suggesting the reduction of the ceria domains. It is worth mentioning that a much weaker, yet visible negative feature was also observed in analogous experiments performed on 20Ba/Pt/Ba/Al catalyst (data not shown) indicating that the 3695 cm^{-1} feature in Fig. 8 is associated with both alumina and reduced ceria domains. However noticeably stronger negative 3695 cm^{-1} feature for the 20Ba/Pt/20Ce/Al surface indicates that this feature can still be used to monitor the extent of ceria reduction in a qualitative manner. After the H_2 reduction at 573 K, almost all of the nitrate signals vanish (Fig. 8a), along with further dehydroxylation and ceria reduction (Fig. 8c).

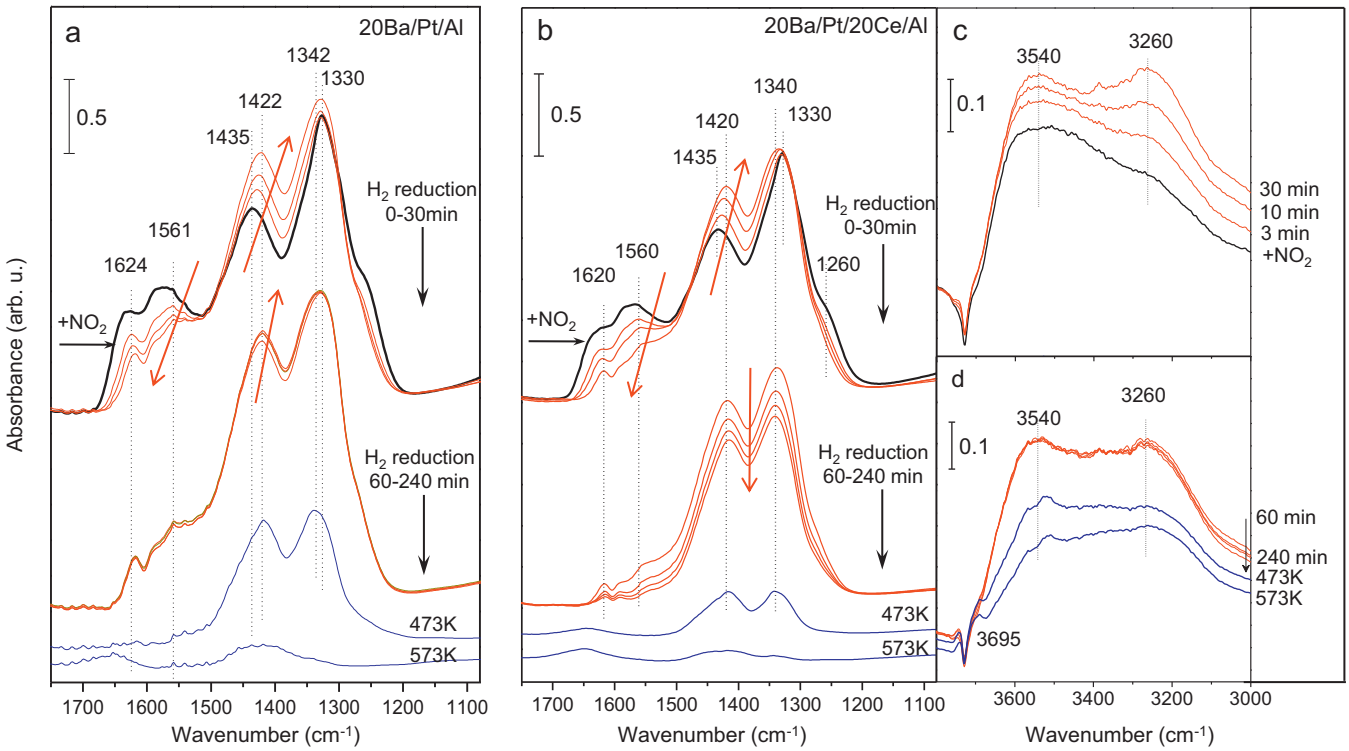

Fig. 8. Time-dependent in situ FTIR spectra corresponding to NO_2 adsorption and saturation (5.0 Torr NO_2(g), 10 min, black spectra) followed by subsequent reduction with H_2(g) (15.0 Torr H_2(g), 3, 10, 30, 60, 120, 180, 240 min, red spectra) on (a) 20Ba/Pt/Al (b) 20Ba/Pt/20Ce/Al samples at 323 K. Blue spectra were obtained after the 240 min reduction period by increasing the sample temperature to 473 K and 573 K in H_2(g), respectively. Panel (a) and (b) present the NO_x regions of the FTIR spectra of 20Ba/Pt/Al and 20Ba/Pt/20Ce/Al, respectively. Panels (c) and (d) correspond to –OH/–NH stretching region of 20Ba/Pt/20Ce/Al. All spectra were acquired at 373 K. Black spectra were acquired in vacuum while red and blue spectra were acquired in H_2(g). (For interpretation of the references to color in this figure legend, the reader is referred to the web version of this article.)

3.4. Direct evidence for the enhancement of H_2 activation upon ceria promotion: H_2-TPR analysis

In order to provide a direct evidence for the enhancement of the H_2 activation by ceria promoted NSR catalysts under flow conditions, we also performed H_2 TPR experiments on 20Ba/Pt/Ba/Al and 20Ba/Pt/20Ce/Al samples in a comparative manner (Fig. 9).

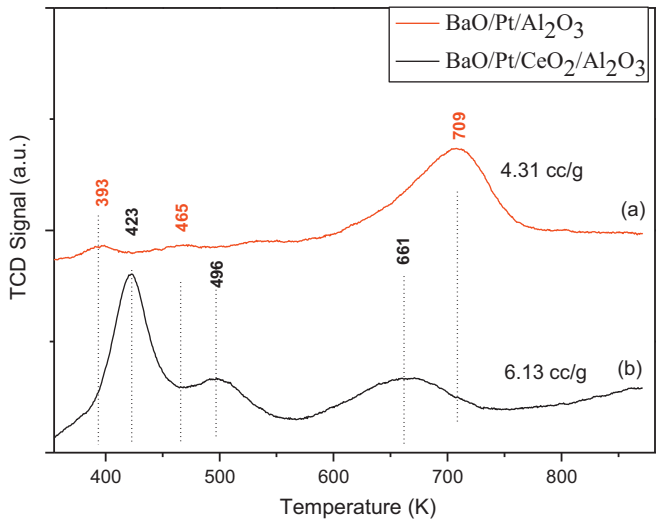

Fig. 9. TPR profiles of $BaO/Pt/Al_2O_3$ (red) and $BaO/Pt/CeO_2/Al_2O_3$ (black) under 10% H_2 balanced with Ar while the temperature was raised from 323 K to 873 K at a rate of 10 K/min. (For interpretation of the references to color in this figure legend, the reader is referred to the web version of this article.)

Ceria is known to have two characteristic TPR features at 673 and 973 K. While the former TPR feature is attributed to reduction of surface oxygen, latter feature is related to reduction of the lattice oxygen [48–50]. Ceria-promoted NSR catalyst (i.e. $BaO/Pt/20CeO_2/Al_2O_3$) in Fig. 9 reveals three main TPR signals at 423, 496 and 661 K. The 423 K signal can be attributed to the reduction of PtO_x species on ceria and the reduction of ceria in the close proximity of the Pt sites [51,52]. The low temperature shoulder at <393 K can be associated with the reduction of PtO_x located on alumina surface. The 496 K signals are tentatively assigned to the reduction of bridging oxygen (Pt–O–Ce) sites in the Pt/CeO_x heterojunctions. Furthermore, the TPR signal for the $BaO/Pt/20CeO_2/Al_2O_3$ sample located at 661 K can be assigned to the reduction of ceria domains on the surface which are not in direct contact with the Pt sites. The presence of intense TPR features for this sample at $T < 550$ K is consistent with a high Pt dispersion on the ceria promoted sample.

TPR trace for the conventional NSR catalyst (i.e. $BaO/Pt/Al_2O_3$) in Fig. 9, displays two weak features at 393 and 465 K as well as a stronger feature at 709 K. TPR signals at 393 and 465 K can be attributed to the reduction of oxidized Pt species. On the other hand, the high temperature signal at 709 K can be associated with reduction of BaO_2 species and/or decomposition of $BaCO_3$, where CO_2 evolving from carbonate decomposition can consume hydrogen via the reverse water-gas shift reaction catalyzed by Pt [52].

Comparison of the total H_2 consumption during the TPR experiments for the 20Ba/Pt/Ba/Al and 20Ba/Pt/20Ce/Al samples reveals that while the conventional NSR catalyst consumed 4.31 cc/g H_2 during the TPR, ceria-promoted NSR catalyst consumed 6.13 cc/g. These results are in perfect agreement with the previously discussed structural characterization and in situ spectroscopic data suggesting that ceria-promoted NSR catalysts reveal novel catalytic

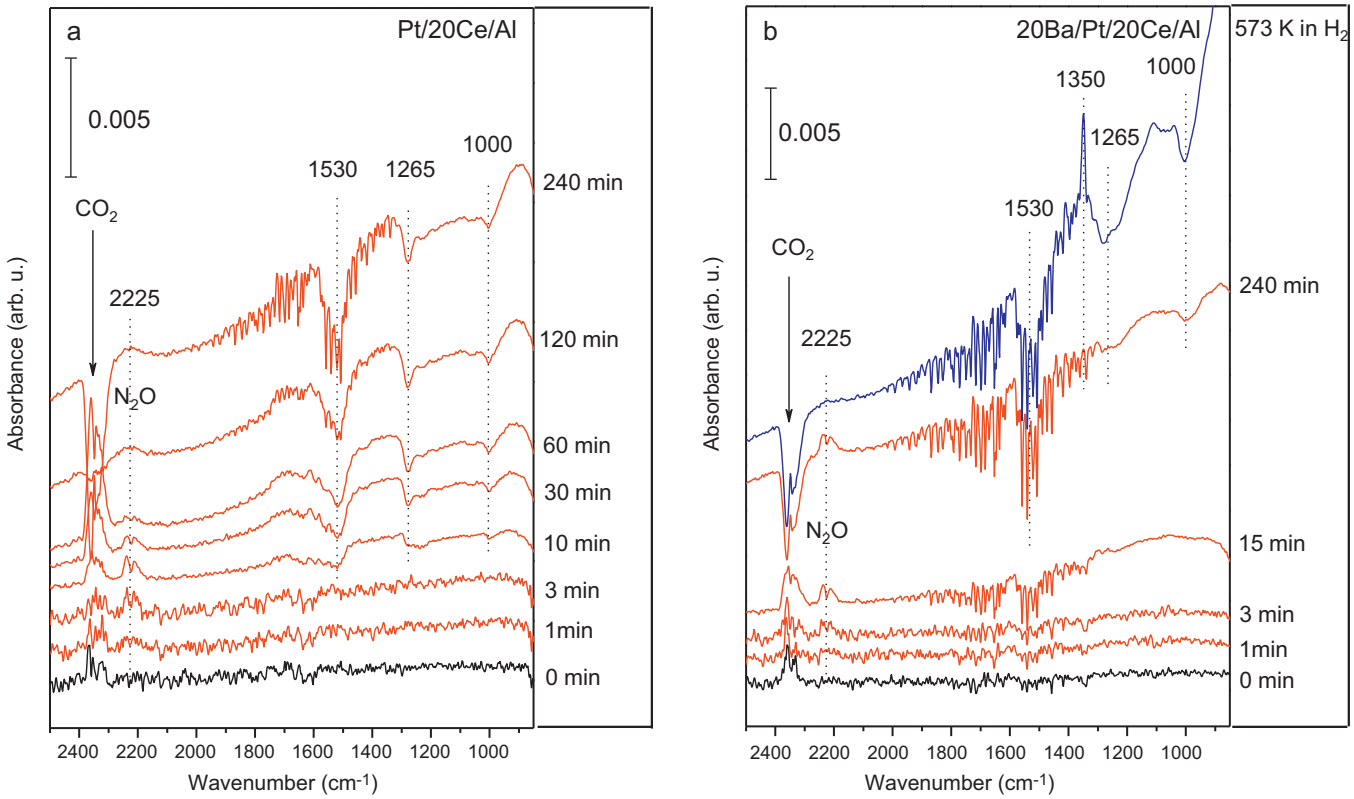

Fig. 10. Time-dependent in situ gas phase FTIR spectra corresponding to NO_2 adsorption and saturation (5.0 Torr NO_2(g), 10 min, black spectra) followed by subsequent reduction with H_2(g) (15.0 Torr H_2(g), red spectra) on (a) Pt/20Ce/Al and (b) 20Ba/Pt/20Ce/Al at 323 K. Blue spectrum in panel (b) was obtained after the 240 min reduction period by increasing the sample temperature to 573 K in H_2(g). All spectra were acquired at 373 K. Black spectra were acquired in vacuum while red and blue spectra were acquired in H_2(g). (For interpretation of the references to color in this figure legend, the reader is referred to the web version of this article.)

sites which do not only boost the total amount of activated hydrogen on the surface but also decrease the thermal threshold for nitrate reduction.

3.5. Monitoring reduction products via gas phase FTIR spectroscopy

Finally, time dependent evolution of the gas phase products during the reduction of NO_x-saturated (and subsequently evacuated) Pt/20Ce/Al and 20Ba/Pt/20Ce/Al via H_2(g) was also monitored by using gas phase FTIR spectroscopy at 323 K (Fig. 10a and b, respectively). During these experiments, catalyst samples inside the FTIR reactor was moved above the IR beam, preventing the detection of surface IR signals originating from the catalyst samples. It is seen in Fig. 10a that N_2O(g) (i.e. 2225 cm^{-1} feature) immediately becomes visible as the only detectable gas phase reaction product via FTIR over the Pt/20Ce/Al sample in the first 3 min of the reduction period. N_2O(g) signal continues to increase in the first 10 min of the reduction period and then starts to decrease. It is likely that the attenuation of the N_2O(g) signal is accompanied by the further reduction of N_2O(g) to N_2(g), a species which is invisible in gas phase FTIR. This observation is in agreement with the corresponding surface FTIR data presented in Fig. 7b, showing that after the 4 hr reduction period at 323 K on the Pt/20Ce/Al sample, a large portion of the stored NO_x species are eliminated. Thus, it is apparent that the eliminated nitrate species from the Pt/20Ce/Al surface at 323 K are first converted into N_2O(g) and then to N_2(g). In addition, formation of H_2O(g) (1620 cm^{-1}) is also visible in the FTIR spectra acquired between 10–240 min of the reduction period (Fig. 10a). Besides these features, other spectral artifacts are also observed in Fig. 10a, namely the progressively growing negative features located at 1530, 1265 and 1000 cm^{-1} which are associated with the elimination of the monodentate nitrates chemisorbed on the IR-transparent BaF_2 windows of the FTIR reactor during the reduction process.

Fig. 10b reveals that N_2O(g) and H_2O(g) are the only detectable reduction products during the reduction of the NO_x-saturated 20Ba/Pt/20Ce/Al NSR catalyst at 323 K via H_2(g). It is also visible in Fig. 10b that even after a 4 h reduction period, N_2O(g) still exists in the reactor and not completely converted into N_2. This observation is in good accordance with the surface FTIR data given in Fig. 8a revealing that after the 4 h reduction period at 323 K, a significantly large portion of the nitrate species are present on the 20Ba/Pt/20Ce/Al surface which can constantly supply N_2O(g) into the reactor. Thus, for a complete removal/reduction of the N_2O(g) species, stronger reduction conditions are required. This was also accomplished by increasing the 20Ba/Pt/20Ce/Al sample temperature quickly to 573 K in the presence of H_2(g) after the 4 hr reduction period (topmost spectrum in Fig. 10b). Clearly, these strongly reducing conditions can readily eliminate all of the N_2O(g) signal by presumably producing N_2(g). Note that the sharp spectral artifact located at 1350 cm^{-1} in Fig. 10b, which is formed immediately after increasing the sample temperature to 573 K is due to the formation of bulk nitrates on the BaF_2 windows of the FTIR reactor as a result of the rapid NO_x desorption/breakthrough from the catalyst surface.

4. Conclusions

In the current work, NO_x storage and the subsequent reduction of the stored NO_x species via H_2(g) were investigated over ceria-promoted NSR catalysts (i.e. 20Ba/Pt/20Ce/Al). A systematic

approach was followed in order to elucidate the catalytic function of the individual structural components constituting the catalyst formulation by investigating γ-Al_2O_3, 20Ba/Al, 20Ce/Al, 20Ba/20Ce/Al, 8Ba/20Ce/Al, Pt/Al, Pt/20Ce/Al, 20Ba/Pt/Al and 20Ba/Pt/20Ce/Al samples in a comparative manner.

SMSI between Pt sites and the $BaO/BaO_2/CeO_x/CeO_2$ domains were observed leading to a complex redox interplay including the oxidation of the precious metal sites, reduction of ceria, formation of BaO_2 species as well as the formation of Pt–O–Ce interfacial sites on the 20Ba/Pt/20Ce/Al surface which seem to have a vital role in the NO_x storage and reduction chemistry. Ceria domains also act as anchoring sites for Pt species, limit their surface diffusion, enhance dispersion and hinder sintering at elevated temperatures.

On the Ba/Pt/Ce/Al catalyst surface, reduction of the stored nitrates under relatively mild conditions via H_2(g) initially leads to formation of surface nitrites, –OH and –NH_x surface species and gas phase N_2O, as well as the destruction of surface nitrate species, leaving bulk nitrates mostly intact. Reduction proceeds with the conversion of N_2O(g) into N_2(g) along with the partial loss of surface –OH and –NH_x groups, dehydration and the loss of bulk nitrates.

Formation of oxygen vacancies in the ceria lattice accompanies the NO_x reduction process. Although ceria promotion does not seem to have a substantial influence on the overall NO_x storage capacity, it does have a clearly positive impact on the NO_x reduction which is associated with enhancement in the total amount of activated hydrogen on the catalyst surface and lowering of the thermal threshold for hydrogen activation.

Acknowledgements

Authors gratefully acknowledge Dr. Chang Hwan Kim and Dr. Wei Li of General Motors Global Research and Development (Warren, MI) for performing the TPR experiments and for fruitful discussions about the experimental results. E.O. acknowledges support from Turkish Academy of Sciences (TUBA) through the "Outstanding Young Investigator" grant. E.V. and V.B. acknowledge RFBR (Russia) #12-03-91373-CT_a for financial support. Authors also thank Margarita Kantcheva for fruitful discussions.

Appendix A. Supplementary data

Supplementary data associated with this article can be found, in the online version, at http://dx.doi.org/10.1016/j.apcatb.2013.04.075.

References

[1] K. Kato, H. Nohira, K. Nakanishi, S. Iguchi, T. Kihara, H. Muraki, Eur Patent application 0,573,672 A1, 1993.
[2] N. Myioshi, S. Matsumoto, K. Katoh, T. Tanaka, K. Harada, N. Takahashi, K. Yokota, M. Sugiura, K. Kasahara, SAE Technical Papers Series No. 950809, 1995.
[3] L. Lietti, P. Forzatti, I. Nova, E. Tronconi, Journal of Catalysis 204 (2001) 175.
[4] O. Mekasuwandumrong, P. Praserthdam, M. Inoue, V. Pavarajarn, W. Tanakulrungsank, Journal of Material Science 39 (2004) 2417.
[5] S.H. Cai, S.N. Rashkeev, S.T. Pantelides, K. Sohlberg, Physical Review B 67 (2003) 224104.
[6] F. Rohr, S.D. Peter, E. Lox, M. Kogel, A. Sassi, L. Juste, C. Rigaudeau, G. Belot, P. Gelin, M. Primet, Applied Catalysis B: Environmental 56 (2005) 201.
[7] M. Casapu, J. Grunwaldt, M. Maciejewski, M. Wittrock, U. Gobel, A. Baiker, Applied Catalysis B: Environmental 63 (2006) 232.
[8] C.T. Campbell, Nature Chemistry 4 (2012) 597.
[9] A. Bruix, J.A. Rodriguez, P.J. Ramirez, S.D. Senanayake, J. Evans, J.B. Park, D. Stacchiola, P. Liu, J. Hrbek, F. Illas, Journal of American Chemical Society 134 (2012) 8968.
[10] J.A. Rodriguez, P. Liu, J. Hrbek, J. Evans, M. Perez, Angewandte Chemie International Edition 46 (2007) 1329.
[11] S. Ozkara-Aydinoglu, E. Ozensoy, E.A. Aksoylu, International Journal of Hydrogen Energy 34 (2009) 971.
[12] Y. Nagai, T. Yamamoto, T. Tanaka, S. Yoshida, T. Nonaka, T. Okamoto, A. Suda, M. Sugiura, Catalysis Today 74 (2002) 225.
[13] J.Z. Shyu, W.H. Weber, H.S. Ghandi, Journal of Physical Chemistry 92 (1988) 4964.
[14] V.V. Pushkarev, V.I. Kovalchuk, J.L. d'Itri, Journal of Physical Chemistry B 108 (2004) 5341.
[15] K. Nakamoto, Infrared and Raman Spectra of Inorganic and Coordination Compounds, 4th edition, Wiley, New York, 1988.
[16] E.I. Vovk, E. Emmez, M. Erbudak, V. Bukhtiyarov, E. Ozensoy, Journal of Physical Chemistry C 115 (2011) 24256.
[17] S.M. Andonova, G.S. Şentürk, E. Kayhan, E. Ozensoy, Journal of Physical Chemistry C 113 (2009) 11014.
[18] S.M. Andonova, G.S. Şentürk, E. Ozensoy, Journal of Physical Chemistry C 114 (2010) 17003.
[19] E. Kayhan, S.M. Andonova, G.S. Şentürk, C.C. Chusuei, E. Ozensoy, Journal of Physical Chemistry C 114 (2010) 357.
[20] W.H. Weber, G.W. Graham, J.R. Mc Bride, Physical Review B 42 (1990) 10969.
[21] W. Lin, A.A. Herzing, C.J. Kiely, I.E. Wachs, Journal of Physical Chemistry C 112 (2008) 5942.
[22] M.S. Brogan, J. Dines, A. Cairns, Journal of the Chemical Society, Faraday Transactions 90 (1994) 1461.
[23] L.L. Murrel, S.J. Tauster, D.R. Anderson, Studies in Surface Science and Catalysis 71 (1991) 275.
[24] Y. Nagai, T. Hirabayashi, K. Dohmae, N. Takagi, T. Minami, H. Shinjoh, S. Matsumoto, Journal of Catalysis 242 (2006) 103.
[25] A.F. Diwell, R.R. Rajaram, H.A. Shaw, T.J. Truex, Studies in Surface Science and Catalysis 71 (1991) 139.
[26] H.C. Yao, Y.F.Y. Yao, Journal of Catalysis 86 (1984) 254.
[27] J.G. Nunan, M.J. Cohn, J.T. Donner, Catalysis Today 14 (1992) 277.
[28] A. Trovarelli, G. Dolcetti, C. de Leitenburg, J. Kaspar, Studies in Surface Science and Catalysis 75 (1993) 2781.
[29] S.J. Tauster, Accounts of Chemical Research 20 (1987) 389.
[30] J.A. Farmer, C.T. Campbell, Science 329 (2010) 933.
[31] C. Hess, J.H. Lunsford, Journal of Physical Chemistry B 106 (2002) 6358.
[32] B. Westerberg, E. Fridell, Journal of Molecular Catalysis A: Chemical 165 (2001) 249.
[33] Ch. Sedlmair, K. Seshan, A. Jentys, J.A. Lercher, Journal of Catalysis 214 (2003) 308.
[34] E. Ozensoy, D. Herling, J. Szanyi, Catalysis Today 136 (2008) 46.
[35] A. Trovarelli, Catalysis Reviews: Science and Engineering 38 (1996) 439.
[36] G. Busca, Catalysis Today 27 (1996) 457.
[37] A. Davydov, Molecular Spectroscopy of Oxide Catalyst Surfaces, Wiley, USA, 2003, pp. 81–83.
[38] T.A. Gordymova, A.A. Davydov, Journal of Applied Spectroscopy 39 (1983) 621.
[39] J.H. Kwak, D. Mei, Ch-W. Yi, D.H. Kim, C.H.F. Peden, F. Allard, Journal of Catalysis 261 (2009) 17.
[40] J. Szanyi, J.H. Kwak, D.H. Kim, S.D. Burton, C.H.F. Peden, Journal of Physical Chemistry B 109 (2005) 27.
[41] T. Venkov, K. Hadjiivanov, D. Klissurski, Physical Chemistry Chemical Physics 4 (2002) 2443.
[42] J. Szanyi, J.H. Kwak, R.J. Chimentao, C.H.F. Peden, Journal of Physical Chemistry C 111 (2007) 2661.
[43] M. Digne, P. Sautet, P. Raybaud, P. Euzen, H. Toulhoat, Journal of Catalysis 226 (2004) 54.
[44] J.H. Kwak, J.Z. Hu, D.H. Kim, J. Szanyi, C.H.F. Peden, Journal of Catalysis 251 (2007) 189.
[45] G.S. Şentürk, E.I. Vovk, V.I. Zaikovskii, Z. Say, A.M. Soylu, V.I. Bukhtiyarov, E. Ozensoy, Catalysis Today 184 (2012) 54.
[46] T. Szailer, J.H. Kwak, D.H. Kim, J.C. Hanson, C.H.F. Peden, J. Szanyi, Journal of Catalysis 239 (2006) 51.
[47] J. Szanyi, J.H. Kwak, D.H. Kim, X. Wang, R.J. Chimentao, J. Hanson, W.S. Epling, C.H.F. Peden, Journal of Physical Chemistry C 111 (2007) 4678.
[48] H.C. Yao, Y.F.Y. Yao, Journal of Catalysis 86 (2) (1984) 254–265.
[49] G. Jacobs, U.M. Graham, E. Chenu, P.M. Patterson, A. Dozier, B.H. Davis, Journal of Catalysis 229 (2) (2005) 499–512.
[50] S. Ricote, G. Jacobs, M. Milling, Y.Y. Ji, P.M. Patterson, B.H. Davis, Applied Catalysis A: General 303 (1) (2006) 35–47.
[51] M.J. Tiernan, O.E. Finlayson, Applied Catalysis B: Environmental 19 (1998) 23–35.
[52] C. Shi, Y. Ji, U.M. Graham, G. Jacobs, M. Crocker, Z. Zhang, Y. Wang, T.J. Toops, Applied Catalysis B: Environmental 119–120 (2012) 183–196.